NANO LETTERS

Letter

pubs.acs.org/NanoLett

# Effects of Thickness on the Metal−Insulator Transition in Free-Standing Vanadium Dioxide Nanocrystals

Mustafa M. Fadlelmula,[†,‡] Engin C. Sürmeli,[†,‡] Mehdi Ramezani,[†,‡] and T. Serkan Kasırga*[,†,‡,§]

[†]National Nanotechnology Research Center, [‡]Institute of Materials Science and Nanotechnology, and [§]Department of Physics, Bilkent University, Bilkent, Ankara 06800, Turkey

Supporting Information

**ABSTRACT:** Controlling solid state phase transitions via external stimuli offers rich physics along with possibilities of unparalleled applications in electronics and optics. The well-known metal−insulator transition (MIT) in vanadium dioxide ($VO_2$) is one instance of such phase transitions emerging from strong electronic correlations. Inducing the MIT using electric field has been investigated extensively for the applications in electrical and ultrafast optical switching. However, as the Thomas−Fermi screening length is very short, for considerable alteration in the material's properties with electric field induced MIT, crystals below 10 nm are needed. So far, the only way to achieve thin crystals of $VO_2$ has been via epitaxial growth techniques. Yet, stress due to lattice mismatch as well as interdiffusion with the substrate complicate the studies. Here, we show that free-standing vapor-phase grown crystals of $VO_2$ can be milled down to the desired thickness using argon ion-beam milling without compromising their electronic and structural properties. Among our results, we show that even below 4 nm thickness the MIT persists and the transition temperature is lowered in two-terminal devices as the crystal gets thinner. The findings in this Letter can be applied to similar strongly correlated materials to study quantum confinement effects.

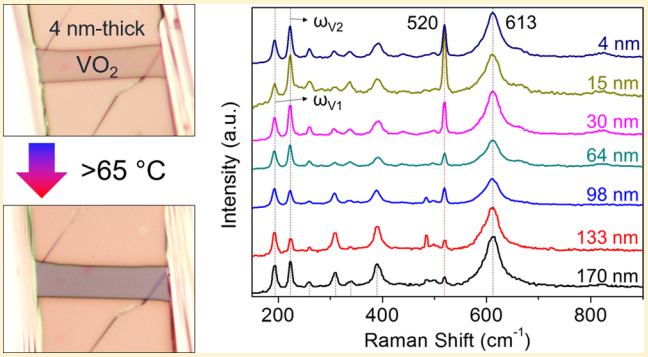


**KEYWORDS:** *Vanadium dioxide, strongly correlated materials, metal−insulator transition, argon ion beam milling*

Exotic solid state phase transitions emerging from strong correlation effects are remarkably sensitive to external as well as internal stimuli. This marked sensitivity, combined with first-order nature of the phase transitions, makes it notoriously challenging to study and control these phenomena. Metal−insulator transition (MIT) in vanadium dioxide ($VO_2$) is an example of such first-order phase transitions emerging from strong electronic correlations.[1] The MIT takes place at a critical temperature, $T_C$, of 65 °C in free-standing crystals[2] and can be tuned via external stimuli such as strain and doping.[3−6] During MIT, the high-temperature metallic phase (rutile, R) turns into a low temperature insulating phase (monoclinic, M1). One promising application of the MIT is the demonstration of a novel field effect transistor based on the electrical induction of this phase transition[7] for electrical and ultrafast optical switching.[8,9] However, Thomas−Fermi screening length, $L_{T-F}$, possesses a limit on the channel thickness for achieving on/off ratio of the observed 5 orders of magnitude change in the conductivity at the MIT in free single-crystals of $VO_2$. An estimate of $L_{T-F}$ using the parameters in the literature, ranges from 0.7 to 6.0 nm in the insulating phase (see the Supporting Information).[10−13] Thus, thin crystals of $VO_2$ are needed for the investigation of the effect of thickness on the MIT for a successful demonstration of electric field-induced phase transition.

So far, the only way to achieve sub-10 nm thin single-crystals of $VO_2$ has been via epitaxial growth methods. There are many studies in the literature investigating the effects of film thickness on the MIT in epitaxially grown single-crystal $VO_2$. However, all these studies are impaired due to stress caused by lattice mismatch between the film and the substrate.[14−16] Further complication in the properties of such sub-5 nm $VO_2$ films comes from interdiffusion of vanadium and titanium at the $VO_2$−$TiO_2$ interface.[17−20] There are various studies on ultrathin sputtered films as well, yet the polycrystalline nature of these films makes it impossible to study the effect of crystal thickness on the MIT.[21−23] An alternative approach would be using vapor-phase deposited $VO_2$ nanocrystals. However, there is limited control over the crystal thickness in the vapor-phase deposition method, and the typical minimum crystal dimensions are no less than 30 nm.[24,25]

In this Letter, we report a method to mill vapor-phase deposited $VO_2$ nanocrystals to the desired thickness for the first time, using argon ion beam milling. We investigate the structural and electronic properties of the milled nanobeams. Figure 1a shows vapor-phase deposited $VO_2$ nanoplates and

**Received:** December 6, 2016
**Revised:** February 1, 2017
**Published:** February 21, 2017





DOI: 10.1021/acs.nanolett.6b05067
*Nano Lett.* 2017, 17, 1762−1767

nanobeams grown on an oxidized silicon chip exposed to Ar-ions for 10 min while one-half is protected by a photoresist layer.

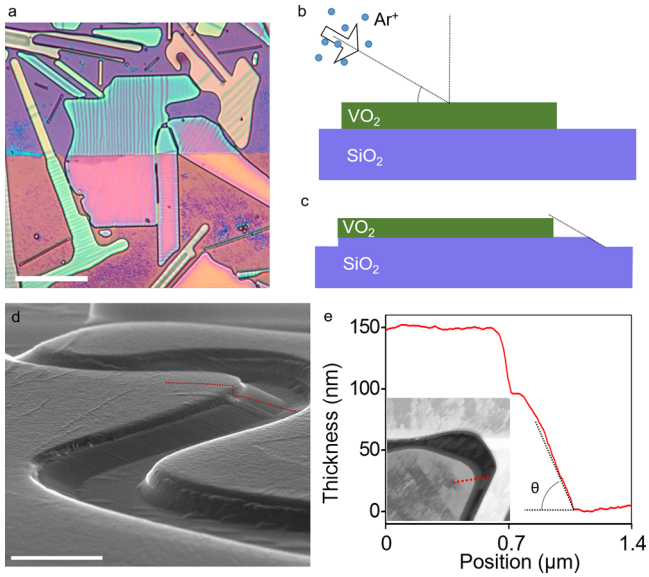


**Figure 1.** (a) $VO_2$ platelets on an oxidized silicon chip after 10 min of etching. The upper half of the sample was covered with photoresist to leave a pristine surface for thickness reference. The image is taken at 66 °C, after the photoresist has been removed. Scale bar is 20 $\mu$m. (b) Schematic of ballistic Ar-ions aimed at a $VO_2$ crystal at an oblique angle. (c) After milling, the $VO_2$ crystal gets thinner by leaving a terrace on the side opposing the ion gun. (d) SEM image shows a typical example of the terrace formed behind the crystal. Scale bar is 2 $\mu$m. AFM height trace given in (e) is taken over the red dashed line overlaid on the SEM micrograph. Inset shows the false color height map of the same region captured in the SEM micrograph. Angle $\theta$ indicated on the height trace, although exaggerated in the graph as lateral dimensions and the height are not on the same scale, matches with the ion gun pointing angle.

Argon ion milling etch rate is critical to prepare samples reproducibly especially below 10 nm in thickness. To determine the etch rate, some part of the $VO_2$ crystal and/or the $SiO_2$ surface nearby needs to be left unetched as a thickness reference. We use the Ar-ion gun of an X-ray photoelectron spectrometer (XPS) set to 1 keV for etching the samples (see Experimental Methods for details). Since the Ar-ion flux diameter is much larger than the average lateral dimensions of $VO_2$ nanocrystals, it does not have the resolution to leave a pristine surface to be used as a thickness reference in the vicinity of the crystals. The nanocrystals could be partially covered using optical lithography as in Figure 1a, to leave a pristine surface for measuring the etched thickness. However, photoresists we tested are not durable enough for etch durations greater than 10 min. Instead, to have a reference surface we use the fact that the Ar-ion gun is targeted on to the sample surface at an angle $\theta = 32°$. A very narrow strip of $SiO_2$ surface is shadowed by the nanocrystal from the ballistic Ar-ions. Figure 1b, c illustrates the shadowing effect. After etching, this terrace of pristine $SiO_2$ is then used as a reference surface for measuring the etched nanocrystal thickness. Scanning electron microscope (SEM) micrograph of a 28 min etched crystal is shown in Figure 1d. Atomic force microscope (AFM) profile of the same crystal, taken along the red dashed line on the SEM micrograph, is given in Figure 1e. Inset of Figure 1e shows a 2D AFM scan of the same region. The angle of the slope, seen in both the AFM height trace and the SEM micrograph coincides with the Ar-ion gun aiming angle $\theta$. Thickness comparison of eight samples, measured with respect to pristine $SiO_2$ surface before and after etching, reveals an average etch rate of (3.3 ± 0.3) nm/min (see Supporting Information for further details of etch parameters).

Even at Ar-ion beam energies as low as 200 eV, surface damage is inevitable, yet it can be confined to a few nm-thick layer.[26,27] High-resolution transmission electron microscope (HR-TEM) micrograph in Figure 2a shows the cross-section of a 28 min etched $VO_2$ nanoplate (HR-TEM cross sections for different durations are given in the Supporting Information). There is a 5 nm thick amorphous film on the surface of the nanoplate, while the bulk is still single crystal (Figure 2b). We also used SRIM software[28] to simulate the depth of the surface damage, and the results are in agreement with our HR-TEM measurements (see the Supporting Information for SRIM results). To confirm the properties of the bulk of the crystal, we performed micro-Raman spectroscopy (532 nm unpolarized laser excitation) on the milled nanobeams at room temperature. There is no considerable change in the Raman active modes of the M1 phase of $VO_2$ due to milling. For Raman measurements, we transfer $VO_2$ nanobeams on to hexagonal boron nitride (h-BN) flakes before milling to get rid of nonuniform strain due to substrate adhesion.[29] $VO_2$ crystals placed on the surface of h-BN flakes show an abrupt MIT. Thus, the whole crystal is in a single phase at any temperature. As a result, the Raman signal belongs solely to a single phase. Figure 2c shows a typical example.

Raman spectra are taken from an initially 170 nm thick $VO_2$ crystal on an h-BN flake. As the crystal gets thinner, there is a minimal change in the spectrum, except that the Si peak at 520 $cm^{-1}$ from the substrate becomes more pronounced. We observe no shift in the peak positions that are associated with the M1 phase (corresponding peaks are marked with dashed lines in Figure 2c).[30] However, the ratio of intensities of $\omega_{V1}$ (194 $cm^{-1}$) and $\omega_{V2}$ (223 $cm^{-1}$) peaks, $I_{\omega_{V1}}/I_{\omega_{V2}}$, changes, and the 338 $cm^{-1}$ peak becomes more pronounced as the crystal gets thinner. This observation can be explained by the increasing contribution of reflected light from $SiO_2$/Si to the Raman signal. When the nanobeam is thick, a tiny fraction of the intensity is transmitted through the crystal. However, as the nanobeam gets thinner, as it is apparent from the 520 $cm^{-1}$ peak, less light is absorbed by the nanobeam. Reflection from an oxidized silicon substrate has a very strong polarization dependence around the laser excitation wavelength, 532 nm. The P-polarized component of the excitation laser gets reflected about 50 times higher than the S-polarized component.[31] This highly polarized reflected light, upon traveling back through the nanobeam, contributes to the Raman signal leading to a variation in the relative peak intensities. Especially, $I_{\omega_{V1}}/I_{\omega_{V2}}$ and the 338 $cm^{-1}$ peak vary significantly upon change in the polarization of the excitation light.[32] Both Raman and TEM studies indicate that the bulk of the crystal is not affected by the Ar-ion milling.

To analyze the changes caused on the chemical states of the vanadium and the oxygen atoms on the surface of $VO_2$ nanobeams due to the argon ion bombardment, XPS spectra are taken from the samples. We look at three cases; before etching, after etching, and after leaving the etched sample under ambient conditions for 3 days. The XPS survey for vanadium



DOI: 10.1021/acs.nanolett.6b05067
Nano Lett. 2017, 17, 1762−1767

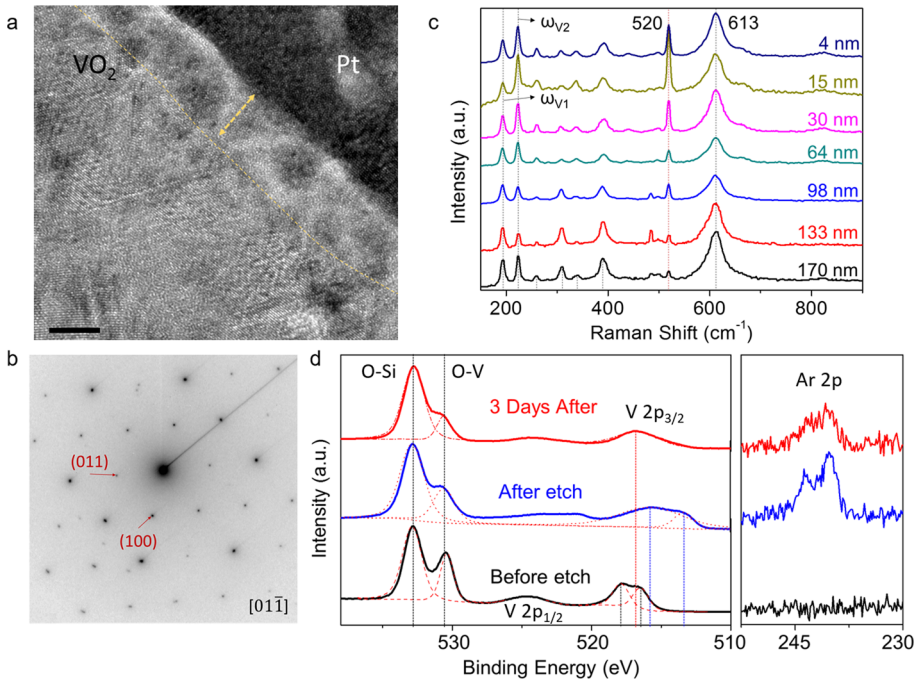


**Figure 2.** (a) HR-TEM image taken through the cross-section of a 28 min etched crystal shows that there is a ~5 nm thick amorphous layer on the surface indicated by the yellow dashed-line and a double-headed arrow. Scale bar is 5 nm. (b) Selected area electron diffraction pattern from the bulk of the same crystal in (a), indexed using the $[00\bar{1}]$ zone axis. (c) Micro-Raman spectra taken from a $VO_2$ nanobeam at various thicknesses are given. A 170 nm thick crystal on h-BN is milled down to 4 nm excluding the amorphous surface film thickness. The 520 $cm^{-1}$ silicon peak, marked with a red dashed line, grows as the crystal gets thinner. Identified Raman peaks corresponding to the M1 phase of $VO_2$ are marked by black dashed lines. In particular $\omega_{V1}$ (194 $cm^{-1}$), $\omega_{V2}$ (223 $cm^{-1}$), and 613 $cm^{-1}$ peaks are marked with long dashed lines to show that there is no shift in their locations for all crystal thicknesses. (d) XPS spectra around oxygen, vanadium, and argon (right panel) binding energies before etching, immediately after etching, and 3 days after etching. Oxygen 1s, vanadium $2p_{1/2}$ and V $2p_{3/2}$, and argon 2p peaks are labeled.

2p peaks and oxygen 1s peaks shows a distinct difference between these three cases (Figure 2d). The sample analyzed in this measurement was grown a few days before the study and kept under ambient conditions until the analysis. XPS spectrum taken before Ar-ion beam milling shows that the nanobeam is oxidized at its surface, as there are two peaks belonging to V $2p_{3/2}$ that are coming from $V_2O_5$ and $V_6O_{13}$.[33] After etching the sample for 28 min, V $2p_{3/2}$ peaks evolve into peaks with binding energy values corresponding to those of $VO_2$ and VO. As some oxygen is removed from the crystals, the intensity of the O 1s (O−V) peak decreases. After leaving the etched sample for 3 days under ambient conditions, there is only one V $2p_{3/2}$ peak left, which is attributed to $V_6O_{13}$. This measurement is consistent with the TEM images, showing that there is an amorphous surface layer poor in oxygen after milling.

We also investigated the possibility of argon entrapment at the sample surface via the 2p peak of argon, as shown in the right panel of Figure 2d. Before etching, we observed no signal, while after etching there are observable peaks associated with argon 2p. However, after 3 days under ambient conditions, argon peaks get weaker, indicating that some of the entrapped argon has escaped. It should be noted that, due to the large spot size of the X-ray beam, XPS surveys not only the $VO_2$ surface but also the $SiO_2$ surface. Based on the XPS spectra, we found that argon entrapment in milled bare $SiO_2$ surface is similar to that of the milled $VO_2$ samples (see Supporting Information). Thus, we conclude that argon entrapment plays an insignificant role in the properties of the milled nanobeams.

Electrical resistance vs temperature (RT) measurements taken from the crystals on h-BN flakes reveal that the critical temperature, $T_C$ decreases as the crystals are milled. For electrical measurements, we place indium contacts at both ends of a crystal on an h-BN flake. Then, AFM is used to determine the initial crystal thickness. Crystal thickness after milling is determined from the etch rate and the etch duration. To minimize the propagation of error in the determination of the thickness, we repeated the AFM measurements after several etch cycles. Since indium pins are placed onto the crystal above $T_C$, a uniform stress along the rutile $c$-axis emanates upon cooling below $T_C$.[34] Thus, although the compressive force, $F$, acting on the crystal by the contacts stays the same as the crystal is milled further, uniaxial compressive stress near the transition temperature, $P_C$, increases. This increase leads to a decrease in $T_C$. Schematic given in the inset of Figure 3a depicts this effect. Compressive strain on the crystal can be expressed as $\eta = \frac{F}{EA}$, where $E$ is Young's modulus and $A$ is the cross-sectional area of the crystal. Using the fact that $\frac{\partial P_C}{\partial T_C} = 71$ MPa °$C^{-1}$ at the M1-R phase boundary,[2] we calculated the expected $T_C$ at a given crystal thickness. As shown in Figure 3a, calculated $T_C$ (blue circles) match well with the measured values (red dots). It should be noted that, depending on the crystal length and width, the strain may be relieved below a certain thickness due to the buckling of the crystal.

Now, we turn our attention to the RT measurements themselves, which are taken from the same type of devices mentioned in the previous paragraph. For each device we study, we first measure the relevant dimensions of the crystals such as the thickness $t$, the width $w$, and the length $l$ to extract the resistivity $\rho$ from RT measurements. After each etching period, the RT measurement is repeated. Notably, after the first etching


DOI: 10.1021/acs.nanolett.6b05067
Nano Lett. 2017, 17, 1762−1767

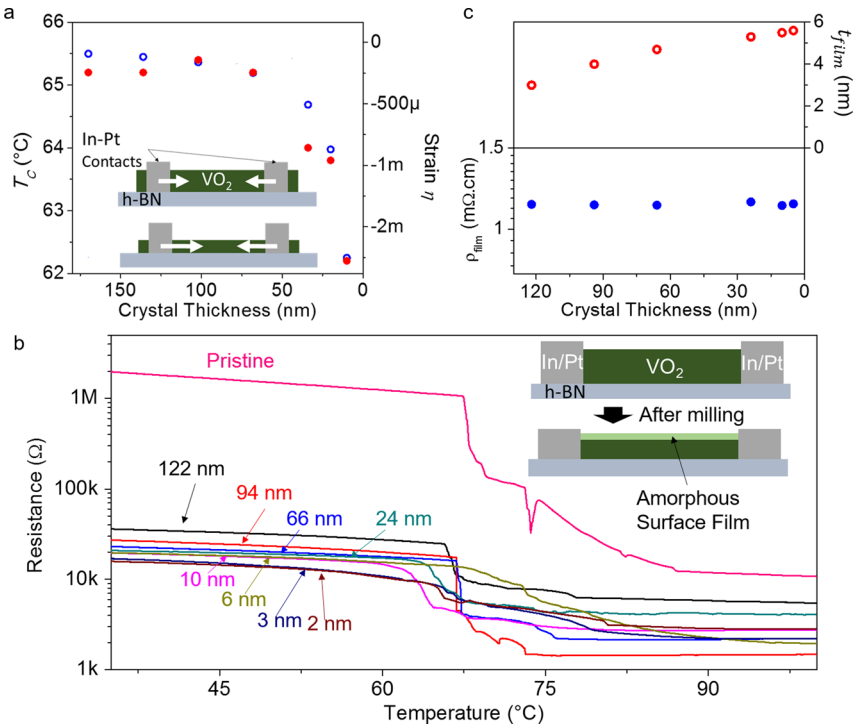


**Figure 3.** (a) Red dots show dependence of the critical temperature, $T_C$, on the crystal thickness for an indium contacted $VO_2$ crystal on h-BN. $T_C$ is measured from the RT graphs. Crystal thickness is determined by AFM measurement before etching. For the consecutive etch durations, the remaining crystal thickness is determined by the etch rate and the etch duration. As the crystal is milled further, $T_C$ decreases due to the increase in compressive strain. Schematic in the inset depicts the increasing compressive strain due to the milling of the crystal. Blue circles are the calculated values for $T_C$. (b) RT measurements are taken from the same crystal after each etch period. The values indicated on the graph are the thicknesses of the nanobeam excluding the amorphous surface film thickness. Inset cartoon depicts the formation of the amorphous surface film after milling. (c) The upper panel shows the thickness of the amorphous surface film, $t_{film}$ (inferred from TEM measurements), with respect to the crystal thickness. As the crystal is milled further, $t_{film}$ increases. The lower panel shows how the resistivity of the amorphous surface film, $\rho_{film}$, changes as the crystal is milled. $\rho_{film}$ is calculated from the measured resistance, crystal length and width, and $t_{film}$.

period, the overall resistance in the insulating phase of the device decreases dramatically, and after each consecutive etch period, the decrease in overall resistance continues at a much slower rate. An exemplary measurement is shown in Figure 3b. This observation can be explained as formation of a conductive amorphous film of vanadium oxides on the crystals as a result of the damage created by the Ar-ion bombardment on $VO_2$ surface as seen in HR-TEM micrographs. The amorphous surface film consists of $VO_2$, VO, and possibly other Magnéli phases of vanadium oxides that are not captured by the analysis of the XPS spectra.

Based on the RT measurement of the pristine sample, we calculate the expected resistance $R^{exp}_{VO_2}$ due to decrease in thickness of the crystal when there would be no conductive amorphous surface film formation. The resistance of the amorphous surface film $R_{surf}$ can be calculated from $R^{exp}_{VO_2}$ and the measured resistance $R_{tot}$ by $\frac{1}{R_{tot}} - \frac{1}{R^{exp}_{VO_2}} = \frac{1}{R_{surf}}$. Thus, the resistivity of the surface film can be calculated by the known length, width, and thickness, $t_{surf}$, of the surface film. Here, we consider that the amorphous surface film thickness increases at a decreasing rate after each etch cycle. As the pristine crystal surface and the amorphous surface film may have different Ar-ion penetration depths, the thickness of the amorphous surface film may increase slightly over increased milling durations. However, during the Ar-ion bombardment as the amorphous surface film gets etched as well, its thickness does not increase at a faster pace. Based on the TEM measurements on crystals etched for different durations and SRIM simulations, we infer that $t_{surf}$ ranges from 3 to 5.6 nm, and this gives a 1.3 mΩ·cm resistivity for the amorphous surface film, $\rho_{film}$, at 35 °C (Figure 3c). This value is consistent with the values reported in the literature for VO and oxygen-poor Magnéli phases.[35,36]

Finally, we focus on removing the amorphous surface film for producing thinned pristine $VO_2$ crystal. SEM micrograph in Figure 4a shows the rough surface of the crystal after 10 min of etching. A dip in 37% hydrochloric acid ($HCl_{(aq)}$), however, removes the amorphous surface film and leaves a pristine $VO_2$ crystal. Figure 4b shows the SEM image taken from the same region after 1 min of HCl treatment. Consistent with the amorphous surface film model we propose, the optical microscope image in Figure 4c shows that the phase transition is still optically visible after 10 nm total crystal is left (about 4 nm of pristine $VO_2$ under the amorphous film), and the MIT takes place as expected from a $VO_2$ crystal strained uniformly along the rutile *c*-axis (see the Supporting Information for a series of pictures of the nanobeam through the MIT). RT measurements also confirm that the removal of the amorphous surface film restores the overall electrical properties of the $VO_2$ crystal. Figure 4d shows measurements taken from the same crystal before Ar-ion etch, after 10 min of etching and after removal of the surface film with HCl. We note that after HCl treatment, resistance of the crystal in the metallic phase is lower than the pristine crystal. This is due to the fact that when the device is dipped in to HCl, indium contacts are etched by the acid. We place indium contacts to the initial contact position on



DOI: 10.1021/acs.nanolett.6b05067
*Nano Lett.* 2017, 17, 1762−1767

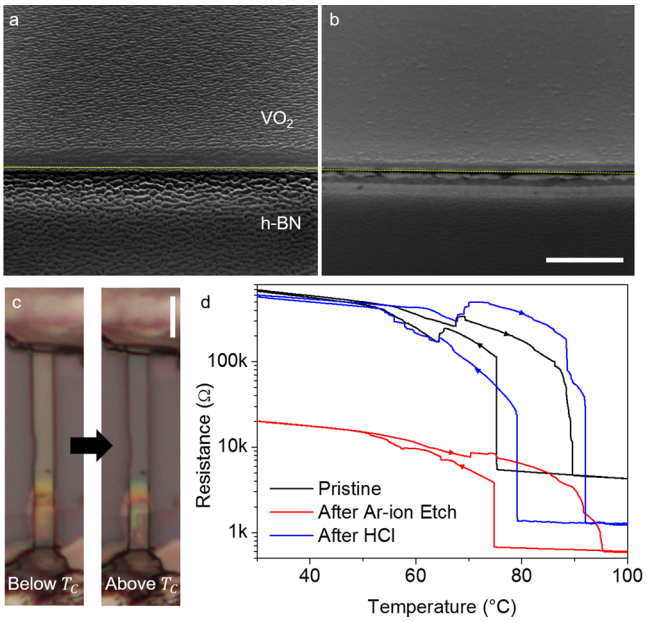


**Figure 4.** (a) SEM micrograph of a $VO_2$ crystal on h-BN on $SiO_2$ shows the surface after 10 min of etching and (b) the same region after the HCl treatment. Yellow dashed line is placed to aid in distinction between $VO_2$ and h-BN. Scale bar is 500 nm. (c) Optical microscope images of a crystal with a total thickness of 10 nm below and above the transition temperature. The rainbow of colors that appear at the lower end of the crystal is due to the buckling of the crystal around that point. See the Supporting Information for other pictures of the device going through the MIT. Scale bar is 10 $\mu$m. (d) Consecutive RT measurements taken from a pristine crystal, after it is etched for 10 min, and after it is treated with HCl for a minute. It is clear from the measurements that, upon removal of the amorphous surface film, most of the electrical properties of the material are restored.

the crystal again for further measurements. Since HCl treatment results in a fresh, nonoxidized $VO_2$ surface, we consider the contact resistance to be lower than the pristine crystal. This leads to a higher change in the resistance through the MIT.

In conclusion, we present a method to mill vapor-phase grow $VO_2$ nanocrystals for the first time and controllably thin the crystals below 10 nm. Our results reveal that the metal–insulator transition still takes place even below 5 nm in free-standing etched nanocrystals. $T_C$ decreases with the crystal thickness in two-terminal devices as a result of the increasing compressive strain. Resistance vs temperature measurements along with the TEM micrographs show the formation of an amorphous conductive surface layer on the crystals, which can be removed by 37% HCl treatment to restore the electrical properties. Overall, the methods developed to produce thin free-standing $VO_2$ crystals in this Letter, could be employed in investigation of high on/off ratio electrical switching applications of the MIT. Unlike a similar approach reported recently on sputtered films of $VO_2$,[23] our work focuses on results from free-standing or predictably strained single crystals, in search of any effects that cannot be explained by strain or similar extrinsic factors. The work presented here could also be applicable for studying quantum confinement effects in strain-free crystals of other similar strongly correlated materials.

**Experimental Methods.** $VO_2$ nanobeams are grown by vapor-phase transport deposition method using $V_2O_5$ powder, placed in the center of a tube furnace in an alumina crucible at 850 °C and low pressure argon carrier gas.[24] The nanobeams are grown on a p-doped (100) Si substrate with 1 $\mu$m thermal oxide coating, elongated along the rutile *c*-axis. The contacts are prepared by placing submicron fine indium pins with a micromanipulator onto the nanobeams heated above 160 °C. Indium pins are drawn from a molten indium with the same micromanipulator used for placing the pins. Ar-ion beam milling is performed using the Ar-ion gun on a K-Alpha X-ray photoemission spectrometer by Thermo Scientific. The Ar-ion gun aimed on to the sample at 32° to the surface and with a 400 $\mu$m flux diameter. We use 1 keV accelerating voltage with medium monatomic flux to minimize Ar-ion implantation into the crystals. Flood gun remains active throughout the milling process to prevent charging of the sample during milling, ensuring a uniform etch rate.

## ■ ASSOCIATED CONTENT

### Supporting Information

The Supporting Information is available free of charge on the ACS Publications website at DOI: 10.1021/acs.nanolett.6b05067.

Experimental details, additional SEM and AFM images (PDF)

## ■ AUTHOR INFORMATION

### Corresponding Author

*E-mail: kasirga@unam.bilkent.edu.tr.

### ORCID

T. Serkan Kasırga: 0000-0003-3510-5059

### Author Contributions

The manuscript was written through contributions of all authors. All authors have given approval to the final version of the manuscript. M.M.F. and T.S.K. performed the experiments. M.R. helped M.M.F. with the experiments. E.C.S. helped with the implementation of the experimental setups and SRIM simulations.

### Notes

The authors declare no competing financial interest.

## ■ ACKNOWLEDGMENTS

This work was supported by the Scientific and Technological Research Council of Turkey (TUBITAK) under grant no: 114F273. Authors thank Abubakar Isa Adamu and Alper Devrim Özkan for their comments on the work.

## ■ REFERENCES

(1) Morin, F. J. *Phys. Rev. Lett.* **1959**, *3* (1), 34–36.
(2) Park, J. H.; Coy, J. M.; Kasirga, T. S.; Huang, C.; Fei, Z.; Hunter, S.; Cobden, D. H. *Nature* **2013**, *500* (7463), 431–434.
(3) Guo, H.; Chen, K.; Oh, Y.; Wang, K.; Dejoie, C.; Asif, S. A. S.; Warren, O. L.; Shan, Z. W.; Wu, J.; Minor, A. M. *Nano Lett.* **2011**, *11* (8), 3207–3213.
(4) Atkin, J. M.; Berweger, S.; Chavez, E. K.; Raschke, M. B.; Cao, J.; Fan, W.; Wu, J. *Phys. Rev. B: Condens. Matter Mater. Phys.* **2012**, *85* (2), 020101.
(5) Aetukuri, N. B.; Gray, A. X.; Drouard, M.; Cossale, M.; Gao, L.; Reid, A. H.; Kukreja, R.; Ohldag, H.; Jenkins, C. A.; Arenholz, E.; Roche, K. P.; Dürr, H. A.; Samant, M. G.; Parkin, S. S. P. *Nat. Phys.* **2013**, *9* (10), 661–666.
(6) Parikh, P.; Chakraborty, C.; Abhilash, T. S.; Sengupta, S.; Cheng, C.; Wu, J.; Deshmukh, M. M. *Nano Lett.* **2013**, *13* (10), 4685–4689.
(7) Chudnovskiy, F.; Luryi, S.; Spivak, B. *Future Trends in Microelectronics: the NanoMillenium*; Wiley, 2002; pp 148–155.



DOI: 10.1021/acs.nanolett.6b05067
*Nano Lett.* 2017, 17, 1762–1767

(8) Cavalleri, A.; Tóth, C.; Siders, C. W.; Squier, J. A.; Ráksi, F.; Forget, P.; Kieffer, J. C. *Phys. Rev. Lett.* **2001**, *87* (23), 237401.
(9) Pashkin, A.; Kübler, C.; Ehrke, H.; Lopez, R.; Halabica, A.; Haglund, R. F.; Huber, R.; Leitenstorfer, A. *Phys. Rev. B: Condens. Matter Mater. Phys.* **2011**, *83* (19), 195120.
(10) Zylbersztejn, A.; Pannetier, B.; Merenda, P. *Phys. Lett. A* **1975**, *54* (2), 145−147.
(11) Yang, Z.; Ko, C.; Balakrishnan, V.; Gopalakrishnan, G.; Ramanathan, S. *Phys. Rev. B: Condens. Matter Mater. Phys.* **2010**, *82* (20), 205101.
(12) Berglund, C. N.; Guggenheim, H. J. *Phys. Rev.* **1969**, *185* (3), 1022−1033.
(13) Liu, K.; Fu, D.; Cao, J.; Suh, J.; Wang, K. X.; Cheng, C.; Ogletree, D. F.; Guo, H.; Sengupta, S.; Khan, A.; Yeung, C. W.; Salahuddin, S.; Deshmukh, M. M.; Wu, J. *Nano Lett.* **2012**, *12* (12), 6272−6277.
(14) Nagashima, K.; Yanagida, T.; Tanaka, H.; Kawai, T. *Phys. Rev. B: Condens. Matter Mater. Phys.* **2006**, *74* (17), 172106.
(15) Yang, T.-H.; Aggarwal, R.; Gupta, A.; Zhou, H.; Narayan, R. J.; Narayan, J. *J. Appl. Phys.* **2010**, *107* (5), 053514.
(16) Passarello, D.; Altendorf, S. G.; Jeong, J.; Samant, M. G.; Parkin, S. S. P. *Nano Lett.* **2016**, *16* (9), 5475−5481.
(17) Muraoka, Y.; Saeki, K.; Eguchi, R.; Wakita, T.; Hirai, M.; Yokoya, T.; Shin, S. *J. Appl. Phys.* **2011**, *109* (4), 043702.
(18) Quackenbush, N. F.; Tashman, J. W.; Mundy, J. A.; Sallis, S.; Paik, H.; Misra, R.; Moyer, J. A.; Guo, J.-H.; Fischer, D. A.; Woicik, J. C.; Muller, D. A.; Schlom, D. G.; Piper, L. F. J. *Nano Lett.* **2013**, *13* (10), 4857−4861.
(19) Paik, H.; Moyer, J. A.; Spila, T.; Tashman, J. W.; Mundy, J. A.; Freeman, E.; Shukla, N.; Lapano, J. M.; Engel-Herbert, R.; Zander, W.; Schubert, J.; Muller, D. A.; Datta, S.; Schiffer, P.; Schlom, D. G. *Appl. Phys. Lett.* **2015**, *107* (16), 163101.
(20) Martens, K.; Aetukuri, N.; Jeong, J.; Samant, M. G.; Parkin, S. S. P. *Appl. Phys. Lett.* **2014**, *104* (8), 081918.
(21) Ham, Y.-H.; Efremov, A.; Min, N.-K.; Lee, H. W.; Yun, S. J.; Kwon, K.-H. *Jpn. J. Appl. Phys.* **2009**, *48* (8), 08HD04.
(22) Yang, Z.; Ramanathan, S. *Appl. Phys. Lett.* **2011**, *98* (19), 192113.
(23) Yamin, T.; Wissberg, S.; Cohen, H.; Cohen-Taguri, G.; Sharoni, A. *ACS Appl. Mater. Interfaces* **2016**, *8*, 14863−14870.
(24) Guiton, B. S.; Gu, Q.; Prieto, A. L.; Gudiksen, M. S.; Park, H. *J. Am. Chem. Soc.* **2005**, *127* (2), 498−499.
(25) Strelcov, E.; Davydov, A. V.; Lanke, U.; Watts, C.; Kolmakov, A. *ACS Nano* **2011**, *5* (4), 3373−3384.
(26) Kato, N. I. *J. Electron Microsc.* **2004**, *53* (5), 451−458.
(27) Matsutani, T.; Iwamoto, K.; Nagatomi, T.; Kimura, Y.; Takai, Y. *Jpn. J. Appl. Phys.* **2001**, *40*, L481.
(28) Ziegler, J. F.; Ziegler, M. D.; Biersack, J. P. *Nucl. Instrum. Methods Phys. Res., Sect. B* **2010**, *268*, 1818−1823.
(29) Wu, J.; Gu, Q.; Guiton, B. S.; de Leon, N. P.; Ouyang, L.; Park, H. *Nano Lett.* **2006**, *6* (10), 2313−2317.
(30) Marini, C.; Arcangeletti, E.; Di Castro, D.; Baldassare, L.; Perucchi, A.; Lupi, S.; Malavasi, L.; Boeri, L.; Pomjakushina, E.; Conder, K.; Postorino, P. *Phys. Rev. B: Condens. Matter Mater. Phys.* **2008**, *44*, 235111.
(31) Diebold, A. C. In Situ Metrology. In *Handbook of Silicon Semiconductor Metrology*; CRC Press: New York, 2001; p 519.
(32) O'Callahan, B. T.; Jones, A. C.; Park, J.-H.; Cobden, D. H.; Atkin, J. M.; Raschke, M. B. *Nat. Commun.* **2015**, *6*, 6849.
(33) Mendialdua, J.; Casanova, R.; Barbaux, Y. *J. Electron Spectrosc. Relat. Phenom.* **1995**, *71* (3), 249−261.
(34) Wei, J.; Wang, Z.; Chen, W.; Cobden, D. H. *Nat. Nanotechnol.* **2009**, *4* (7), 420−424.
(35) Fieldhouse, N.; Pursel, S. M.; Horn, M. W.; Bharadwaja, S. S. N. *J. Phys. D: Appl. Phys.* **2009**, *42* (5), 055408.
(36) Chen, R.-H.; Jiang, Y.-L.; Li, B.-Z. *IEEE Electron Device Lett.* **2014**, *35*, 780−782.



DOI: 10.1021/acs.nanolett.6b05067
*Nano Lett.* 2017, 17, 1762−1767